文章编号 2095-1531(2019)03-0587-09

Characterizing curved surface roughness of Wolter-I X-ray grazing incidence telescope

ZHANG Ya-chao[1,2], LIU Peng[1,2], WANG Xiao-guang[1], HE Ling-ping[1], CHEN Bo[1*]
(1. *Changchun Institute of Optics, Fine Mechanics and Physics, Chinese Academy of Sciences, Changchun* 130033, *China*;
2. *University of Chinese Academy of Sciences, Beijing* 100049, *China*)
* *Corresponding author, E-mail: chenb@ciomp.ac.cn*

Abstract: The X-ray scattering method is investigated in application of characterizing surface roughness of X-ray grazing incidence telescope. The surface figure effect on the scattering diagram of the curved rough mirror is analyzed in detail based on generalized Harvey-Shack surface scatter theory and image formation theory, when smooth-surface approximation is met and the width of the incident beam is about one tenth of spatial wavelength of the surface figure. Based on the analysis, the characterizing scheme is designed and the determination error of the one-dimensional power spectral density function due to the finite width of the receiving slit before the detector is discussed. The scheme is simulated with Zemax and the simulated results verify that the surface figure only affects the measuring accuracy of the low-spatial-frequency surface roughness. The method overcomes difficulty in measuring roughness of the grazing incidence mirror with high resolution conveniently during the development of the X-ray grazing incidence telescope.

Key words: surface scatter; roughness; power spectral density; grazing incidence telescope

X射线散射法测量 Wolter-I 型掠入射望远镜的表面粗糙度

张亚超[1,2],刘 鹏[1,2],王晓光[1],何玲平[1],陈 波[1*]
(1. 中国科学院 长春光学精密机械与物理研究所,吉林 长春 130033;
2. 中国科学院大学,北京,100049)

摘要:研究X射线散射法在软X射线掠入射望远镜反射镜的表面粗糙度测量中的应用。首先,在光滑表面近似和细光束条件下,根据 Harvey-Shack 表面散射理论得出反射镜的面形仅影响总反射光分布中的镜向部分,对散射部分的影响可以忽略不计;然后设计了X射线散射法测量 Wolter-I 型软X射线掠入射望远镜的表面粗糙度的实验方案,并且对引起系统误差的主要因素进行了分析,确定了进行仿真实验时的参数;最后用 Zemax 对实验方案进行了仿真。在空间频率高于

收稿日期:2018-05-18;**修订日期**:2018-06-12
基金项目:国家自然科学基金资助项目(No. U1631117)
Supported by National Natural Science Foundation of China(No. U1631117)

28/mm 时,表面粗糙度的仿真测量结果与真值吻合得非常好。本文研究结果显示:在光滑表面近似和细光束条件下,反射镜的面形仅影响表面粗糙度的低频部分的测量准确性,对高频部分测量准确性的影响可以忽略不计,利用 X 射线散射法可以准确测量软 X 射线掠入射望远镜的表面粗糙度。
关　键　词:表面散射;粗糙度;功率谱密度;掠入射望远镜
中图分类号:O434　　**文献标识码**:A　　doi:10.3788/CO.20191203.0587

1 Introduction

For X-ray/soft X-ray imaging systems, surface roughness is an important factor that directly affects the reflectivity and the optical quality of the grazing incidence mirror. Therefore, it is impossible to fabricate high-quality grazing incidence mirrors without reliably testing surface roughness. Moreover, image degradation due to surface scattering cannot be evaluated without the surface roughness of grazing incidence mirror[1-6]. That is to say, the development of testing methods is necessary and part of the development of X-ray/soft X-ray imaging systems.

Presently, the methods for measuring surface roughness include the mechanical probe scanning method, optical interferometry, using an atomic force microscope (AFM), the optical scattering method etc. State-of-the-art profile instruments, such as optical profilometry and AFM, have a vertical resolution better than one angstrom[6-8]. However, they can only be used to characterize the surface roughness of flat samples[6-9]. In addition, the measuring area of AFMs is very small so the corresponding spatial frequency range is quite narrow. Moreover, the results of AFM and optical surface profiler measurements are very easily affected by surface defects and dust on the sample. The mechanical probe scanning method can be used to characterize the curved surface roughness but it is easy to scratch the sample and its measuring accuracy is limited.

The X-ray scattering method obtains the surface roughness by measuring the angular distribution of the radiation intensity (scattering diagram) scattered by the rough surface[10]. As far as we know, the X-ray scattering method is usually adopted to measure the roughness of a super-smooth plane. For example, in 1988, Alexander Vinogradov first derived the theoretical basis to measure the roughness of a super-smooth plane using the X-ray scattering method[9]. In 2004, V. E. Asadchikov, applied the X-ray scattering method to measure the roughness of a super-smooth plane mirror[10]. In 2010, Wang Yong-gang, studied the X-ray scattering characteristics of a grazing incidence multilayer planar mirror[11]. However, no work has been reported on how to apply the X-ray scattering method to measure the surface roughness of a curved surface. The difficulty in measuring super-smooth curved surface by X-ray scattering method lies in determining how the surface figure affects the scattering diagram of the curved rough mirror.

In section 2, the scattering diagram of a curved rough mirror is derived with consideration to the angular distribution of the radiation intensity due to its surface figure (herein named the surface figure effect) according to the general Harvey-Shack surface scatter theory (GHS) and image formation theory. In section 3, the characterizing scheme for the surface roughness of a secondary mirror is designed. The determination error of the one-dimensional power spectral density (PSD) function due to the width of the receiving slit is evaluated and the optimal width of the detector aperture is obtained. In addition, the scheme is simulated with Zemax by the non-sequence ray tracing method. In section 4, the extracted PSD data is compared with the exact data, which verifies that the surface figure only affects the measuring accuracy of curved surface roughness with low spatial frequency. Finally, some conclusions are given in section 5.

2 Theory about surface figure effect

Consider the light-scattering configuration shown in Fig. 1, where θ_i is the grazing incidence angle, θ and φ are the scattering grazing and azimuth angles and $Z_f(\hat{x}', \hat{y}')$ is the surface figure, respectively. Note that a scaled coordinate system is used, in which $\hat{x} = x/\lambda$, $\hat{y} = y/\lambda$ and $\hat{z} = z/\lambda$. Defining direction cosines

$$\alpha = \cos\theta\cos\varphi,\ \beta = \cos\theta\sin\varphi,\ \gamma = \sin\theta. \quad (1)$$

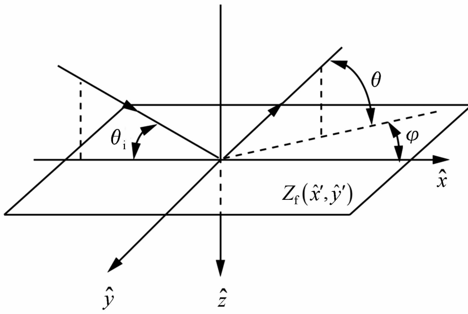

Fig. 1 Schematic diagram of X-rays reflected by a rough surface. θ_i is the grazing incidence angle and θ and φ are the scattering grazing and azimuth angles, respectively

The effect of the surface figure is equivalent to an image forming system that is described by the transfer function according to image formation theory. Therefore, the surface transfer function $H(\hat{x}, \hat{y})$ of an optical component is the product of the figure transfer function $H_f(\hat{x}, \hat{y})$ and the scatter transfer function $H_s(\hat{x}, \hat{y})$, expressed as the following

$$H(\hat{x}, \hat{y}) = H_f(\hat{x}, \hat{y}) \cdot H_s(\hat{x}, \hat{y}). \quad (2)$$

The figure transfer function $H_f(\hat{x}, \hat{y}; 0)$, which is determined by the surface figure is expressed as

$$H_f(\hat{x}, \hat{y}) = \iint_{-\infty} p(\hat{x}', \hat{y}') p(\hat{x}' - \hat{x}, \hat{y}' - \hat{y}) \mathrm{d}\hat{x}\mathrm{d}\hat{y}, \quad (3)$$

where $p(\hat{x}', \hat{y}')$ is the aperture function defined by

$$p(\hat{x}', \hat{y}') = \begin{cases} \exp[\mathrm{i}kZ_f(\hat{x}', \hat{y}')], & (\hat{x}', \hat{y}') \subset \Omega \\ 0. & \text{else} \end{cases}. \quad (4)$$

It is generally accepted that the inverse scattering problem of predicting the surface PSD from the scattering diagram is only possible when the optical surface satisfies the smooth-surface approximation[12-13]:

$$(4\pi\sigma_{\mathrm{rel}}\sin\theta_i/\lambda)^2 << 1, \quad (5)$$

where θ_i is the grazing incidence angle shown in Fig. 1. In these conditions, the scatter transfer function is expressed as

$$H_s(\hat{x}, \hat{y}; \gamma_i, \gamma_s) = A(\gamma_i) + \frac{4\pi^2}{\lambda^4}(\sin\theta_i + \sin\theta)^2 \cdot \frac{\sigma_{\mathrm{rel}}^2}{\sigma_s^2} \cdot C(\hat{x}, \hat{y}), \quad (6)$$

$$A(\gamma_i) = 1 - (2\pi\gamma_i\sigma_{\mathrm{rel}}/\lambda)^2, \quad (7)$$

$$\sigma_{\mathrm{rel}} = \sqrt{\int_{\frac{1}{\lambda}-f_0}^{\frac{1}{\lambda}+f_0} \int_{-\sqrt{\frac{1}{\lambda^2}-(f_x-f_0)^2}}^{\sqrt{\frac{1}{\lambda^2}-(f_x-f_0)^2}} \mathrm{PSD}(f_x, f_y)\,\mathrm{d}f_x\mathrm{d}f_y}, \quad \sigma_s = \sqrt{\int_{-\infty}^{+\infty}\int_{-\infty}^{+\infty} \mathrm{PSD}(f_x, f_y)\,\mathrm{d}f_x\mathrm{d}f_y} \quad (8)$$

$$f_x = \frac{\cos\theta\cos\varphi - \cos\theta_i}{\lambda},\ f_y = \frac{\cos\theta\sin\varphi}{\lambda}, \quad (9)$$

where θ_i is the grazing incidence angle; θ and φ are the grazing and azimuth scattering angles as shown in Fig. 1; σ_{rel} and σ_s are the relevant root-mean-square of the surface roughness and the intrinsic root-mean-square of the surface roughness respectively; PSD (f_x, f_y) is 2-dimension PSD of surface roughness; f_x and f_y are the spatial frequencies.

Since the Fourier transform of the surface transfer function, $H(\hat{x}, \hat{y})$ yields the angle spread function for normal incidence, the radiance distribution for the incident angle, θ_i can be calculated with the shift theorem of Fourier transform theory[13]:

$$\mathrm{ASF}(\alpha,\beta) = F[H(\hat{x},\hat{y})\cdot\exp(-\mathrm{i}2\pi\beta_o\hat{y})] = A(\gamma_i)\mathrm{ASF_f}(\alpha,\beta-\beta_o) + \frac{4\pi^2}{\lambda^4}(\sin\theta_i+\sin\theta)^2\cdot\frac{\sigma_{\mathrm{rel}}^2}{\sigma_s^2}\cdot F[H_f(\hat{x},\hat{y})\cdot C(\hat{x},\hat{y})\cdot\exp(-\mathrm{i}2\pi\beta_o\hat{y})], \tag{10}$$

where $\beta_o = -\beta_i = -\cos\theta_i$.

Furthermore, the spatial wavelength of the surface figure is generally in the range of a few millimeters. The figure transfer function $H_f(\hat{x},\hat{y})$ defined by Eq. (3) is almost unit when the width of the incident beam is close to a tenth of the spatial wavelength. In such circummstances, the angle spread function is expressed as

$$\mathrm{ASF}(\alpha,\beta) = A(\gamma_i)\mathrm{ASF_f}(\alpha,\beta-\beta_o) + \frac{4\pi^2}{\lambda^4}(\sin\theta_i+\sin\theta)^2\cdot\frac{\sigma_{\mathrm{rel}}^2}{\sigma_s^2}\cdot\mathrm{PSD}(f_x,f_y). \tag{11}$$

In fact, the auto-correlation length l (a distance at which the auto-covariance function is reduced to $1/e$, where e is the base of the natural logarithms) is generally in the range of several micrometers to several tens of micrometers, which is much longer than the wavelength of the incident X-ray. Therefore, the relevant root-square-mean surface roughness σ_{rel} is almost equal to the intrinsic root-square-mean surface roughness σ_s. So BRDF is expressed as the following:

$$\mathrm{BRDF}(\theta,\varphi) = Q\cdot A(\gamma_i)\mathrm{ASF_f}(\alpha,\beta-\beta_o) + Q\cdot\frac{4\pi^2}{\lambda^4}(\sin\theta_i+\sin\theta)^2\cdot\mathrm{PSD}(f_x,f_y), \tag{12}$$

where Q is the polar reflectivity

$$Q = \left|\frac{(1-\varepsilon)\sin\theta}{(\sin\theta_i+\sqrt{\varepsilon-\cos^2\theta_i})(\sin\theta+\sqrt{\varepsilon-\cos^2\theta})}\right|^2. \tag{13}$$

In Eq. (13), $\varepsilon=\varepsilon_2/\varepsilon_1$ is the relative dielectric constant of the interface where the subscripts 1 and 2 denote the incident and refracting side, respectively.

Since BRDF is a computed quantity calculated by dividing the measured radiant intensity by the cosine of the scattered angle, the scattering diagram (radiant intensity distribution) is expressed as the following:

$$\Phi(\theta,\varphi) = Q\cdot A(\gamma_i)\cdot\mathrm{ASF_f}(\alpha,\beta-\beta_o)\cdot\sin\theta + Q\cdot\frac{4\pi^2}{\lambda^4}\sin\theta\cdot(\sin\theta_i+\sin\theta)^2\cdot\mathrm{PSD}(f_x,f_y). \tag{14}$$

The scattering diagram is characterized, in general, by two scattering angles (θ,φ). However, as the grazing incidence angle θ_i is typically smaller than the critical angle of the total external reflection θ_c at the wavelength, such a small value of θ_i leads to a large angular difference in the width of the angular distribution of reflected radiation intensity in the incidence ($\delta\theta\sim\lambda/(\pi l\sin\theta_i)$ and in the azimuth ($\delta\theta\sim\lambda/(\pi l)\ll\delta\theta$) planes[9]. In experiments, the scattering diagram is usually integrated over the azimuth angle as:

$$\Pi(\theta) = \int_0^{2\pi}\Phi(\theta,\varphi)\mathrm{d}\varphi. \tag{15}$$

The integrated results could be divided into two parts:

$$\Pi(\theta) = \Pi_f(\theta) + \Pi_s(\theta), \tag{16}$$

where the surface figure $\Pi_f(\theta)$ and the integrated scattering function $\Pi_s(\theta)$ are respectively calculated as the followings:

$$\Pi_f(\theta) = \int_0^{2\pi}Q\cdot A(\gamma_i)\cdot\mathrm{ASF_f}(\alpha,\beta-\beta_o)\cdot\sin\theta\mathrm{d}\varphi, \tag{17}$$

$$\Pi_s(\theta) = Q\cdot\sin\theta\cdot\frac{2\pi^2}{\lambda^3}(\cos\theta_i+\cos\theta)^2\cdot\mathrm{PSD_{1D}}(\mathrm{f_x}). \tag{18}$$

For super smooth optical surfaces, Eq. (16) shows that the surface figure only affects the specular

component, provided that the conditions described above are met. In these conditions, a superposition of the contributions of the figure and the roughness yields the integrated scattering diagram.

3 Characterizing the surface roughness of the X-ray grazing incidence telescope

The space telescope has rigorous requirements on the thermal stability of the mirror body, especially for mirror material. Zerodur has excellent physical and chemical properties such as relatively high strength, a zero-expansion coefficient and high density[11]. Therefore, the soft X-ray space telescope is fabricated with zerodur in our lab. After being polished, the relevant root-mean-square of its surface roughness is usually smaller than 1 nm, which is suitably characterized as being in the soft X-ray band. Tab. 1 lists the parameters of the Wolter-I solar soft X-ray grazing incidence telescope in our laboratory.

Tab. 1 Specifications of solar soft X-ray grazing incidence telescope in our lab

Parameter	Telescope	Paraboloid	Hyperboloid
Nodal focal length/mm	659.885 495		
Optic length/mm		47.5	47.5
Gap about joint/mm	5		
Vertex radius/mm		−2.431 457 33	−2.440 466 51
Inner radius r_{inner}/mm		80.075 946 99	75.414 332 72
Outer radius r_{outer}/mm		81.505 495 11	79.771 451 35
Conic constant ε^2		−1	−1.007 424 25
Location of focus/mm		1 364.867 410 92	705

3.1 Optical design of the measuring system

Since the primary and secondary mirrors are fabricated using the same process, their surface roughness are assumed to be identical[1]. Therefore, only the surface roughness of the primary or secondary mirror need to be characterize. The radiation scattered from the primary mirror is blocked by the secondary mirror while the scattered radiation from the secondary mirror can arrive at the detector without being blocked. Therefore, it is more convenient and suitable to characterize the surface roughness of the secondary mirror.

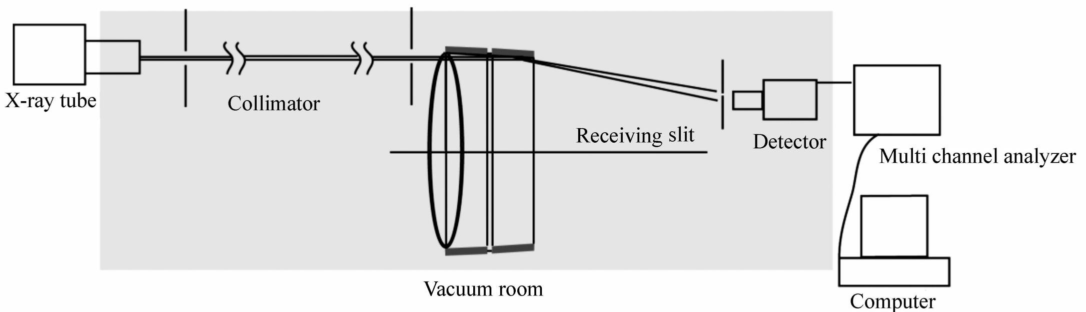

Fig. 2 Schematic diagram for surface roughness characterization

The scheme shown in Fig. 2 is for measuring the surface roughness of the secondary mirror of the solar soft X-ray grazing telescope in our lab. Although, the grazing incidence mirror shown in Fig. 2 is non-nested, the scheme can also be applied to a nested X-ray grazing incidence mirror since each of its shell

can be measured before integration. For the telescope in Tab. 1, the total reflection critical angle θ_c is equal to 5.94° when the incident wavelength λ is equal to 4.47 mm. When the incident radiation is parallel to the optical axis, the grazing incidence angle θ_o of 5.24° is smaller than the total reflection critical angle θ_c. That is to say, the wavelength and the grazing incidence angle are suitable for characterizing the surface roughness.

To condense the information contained in the PSD-function to a few parameters, the K-correlation model of the PSD-function[14] shown in Eq. (19) is used.

$$\mathrm{PSD}(f_x) = \frac{A}{(1+B^2f_x^2)^{C/2}}$$
$$\mathrm{PSD}(f) = \frac{KAB}{(1+B^2f^2)^{(C+1)/2}}. \quad (19)$$
$$K = \frac{1}{\sqrt{2\pi}}\frac{\Gamma[(C+1)/2]}{\Gamma(C/2)}$$

The width of the incident beam is set to 0.2 mm to ensure that Eq. (11) holds true according to the analysis in Sec. 2. The factors causing systematic errors in the determination of the PSD-function include the finite width of the receiving slit before the detector (simply called "receiving slit"), the divergence and spectral width of the incident beam, the noise of the detector etc. In this paper, we will only address the dominant factor and the finite width of the receiving slit in detail. Fig. 3 illustrates the effect of the finite width of the receiving slit.

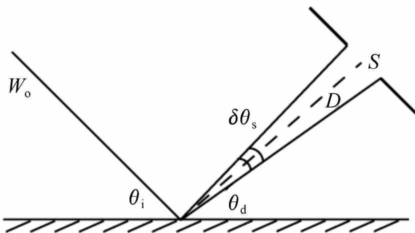

Fig. 3 Error of PSD-function determination caused by the finite width of a receiving slit

For simplicity, the width of the incident beam is ignored and the error of determination of the PSD-function is written as follows[10]:

$$\eta_s \approx \frac{1}{24}\left(\frac{S}{D}\right)^2\frac{1}{\Pi(\theta_d)}\frac{\partial^2\Pi}{\partial\theta^2}(\theta=\theta_d). \quad (20)$$

Dependency of the error η_s on the receiving slit S is shown in Fig. 4. In calculations, we used the following parameters: radiation wavelength $\lambda = 4.47$ nm; grazing incidence angle for the incident beam $\theta_0 = 5.24°$; sample-detector distance $D = 336$ mm. Besides, the PSD-function is supposed to behave in accordance with the fractal-like law as shown in Eq. (19), which is typical for the samples.

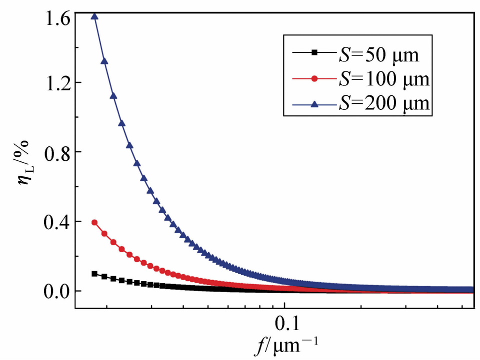

Fig. 4 Error of PSD-function determination η_s for different widths of the receiving slits $S = 50$ μm, 100 μm, 200 μm. Calculations are performed at an incident wavelength of $\lambda = 4.47$ nm, a primary beam grazing incident angle of $\theta_0 = 5.24°$ and a sample-detector distance of $D = 336$ mm

Since the error η_s decreases rapidly with a decrease in the width of the receiving slit as shown in Fig. 4, it is important to minimize the width of the receiving slit. However, when the slit is too narrow, the detected scattered radiation falls sharply and the measured spatial frequency becomes more narrow. As shown in Fig. 5, η_s is less than 0.2% at spatial frequencies larger than 0.02 μm^{-1} when the receiving slit is less than 0.1 mm. According to the above analysis, the error of the PSD function is small when the width of the receiving slit is less than 0.1 mm.

3.2 Simulation

In the simulation, the PSD is modeled by Eq. (19), where $A = 1\ 000.322 \times 10^{-5}$ μm^3, $B =$

12 000 μm and $C = 1.089$. The smooth-surface approximation is satisfied on the simulation. BRDF is calculated from the PSD according to Eq. (12). The characterizing scheme in Sec. 3.1 is designed with Zemax and the simulation is created using the following steps. First, the surface figure effect $\Pi_f(\theta)$, is obtained using the ray tracing method when the secondary mirror surface is perfect. Second, the integrated scattering diagram $\Pi(\theta)$ is obtained using the non-sequential ray-tracing method[15] when the BRDF is added to the secondary mirror. Finally, the PSD function is obtained from Eq. (16).

4 Results and discussion

The simulated results are shown in Fig. 5. Fig. 5(a) shows the scattering diagram of the rough secondary mirror $\Pi(\theta)$, whereas Fig. 5(b) shows the surface figure effect $\Pi_f(\theta)$. The scattered component of the scattering diagram $\Pi_s(\theta)$ is shown in Fig. 5(c), which is obtained by subtracting the surface figure effect $\Pi_f(\theta)$ from the scattering diagram $\Pi(\theta)$. Furthermore, the surface figure effect $\Pi_f(\theta)$, the scattering diagram $\Pi(\theta)$, and the scattered component $\Pi_s(\theta)$ are shown in Fig. 5(d) to demonstrate the surface figure effect on the scattering diagram. As shown in Fig. 5(d), the scattering diagram $\Pi(\theta)$ agrees well with its scattered component $\Pi_s(\theta)$ when the scattering angle is outside the angular range of the surface figure effect $\Pi_f(\theta)$, which verifies that surface figure only affects the specular component of the scattering diagram.

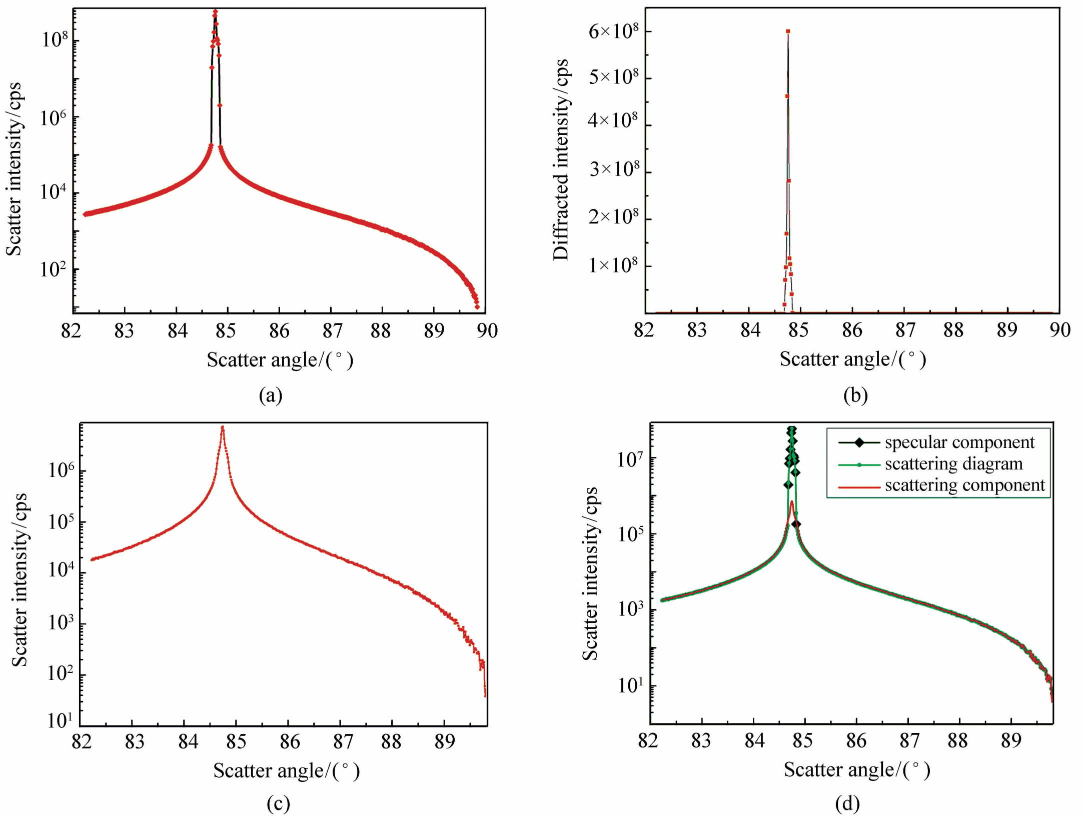

Fig. 5 (a) Scattering diagram, (b) surface figure effect, (c) scattered component of the scattering diagram, (d) analysis of the surface figure effect on the scattering diagram

Fig. 6 shows the PSD data extracted from the scattering diagram $\Pi(\theta)$ and the exact PSD data. The PSD data extracted from the scattering diagram $\Pi(\theta)$ agrees well with the real value (exact PSD da-

ta) when the spatial frequency is more than 28/mm, which confirms that surface figure only affects the measuring accuracy of surface roughness with low spatial frequency. On the other hand, surface roughness with high spatial frequency can be characterized accurately using the X-ray scattering method when smooth-surface approximation is met and the width of the incident beam is about a tenth of spatial wavelength of the surface figure.

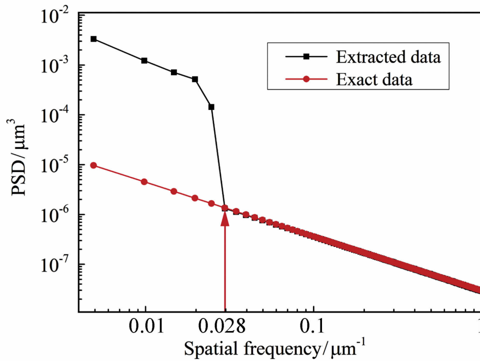

Fig. 6 PSD data extracted from the scattering diagram and its real value

5 Conclusions

In this paper, a theoretical analysis was performed to prove that surface figure only affects the measuring accuracy of the roughness of a curved surface with low frequency when smooth-surface approximation is met and when the width of the incident beam is about a tenth of the spatial wavelength of the surface figure. Based on this analysis, the X-ray scattering method was applied to characterize surface roughness of the secondary mirror of the X-ray grazing incidence telescope. The scheme was simulated with Zemax and the simulated results show that the surface figure only affects the measuring accuracy of the roughness of a curved surface with spatial frequency less than 28/mm, which verifies the accuracy of the theoretical analysis. This method will be valuable and helpful for efficiently developing high quality X-ray imaging systems. It can also be used in other fields, such as modern optics, micro-electronics and micro electro-mechanical systems. The factors causing systematic errors will be analyzed comprehensively in the future.

参考文献:

[1] HARVEY J E, MORAN E C, ZMEK W P. Transfer function characterization of grazing incidence optical systems[J]. *Applied Optics*, 1988, 27(8): 1527-1533.

[2] HARVEY J E. Scattering effects in X-ray imaging system[J]. *Proceedings of SPIE*, 1995, 2515: 246-272.

[3] PETERSON G L. Analytic expression for in-field scattered light distributions[J]. *Proceedings of SPIE*, 2004, 5178: 184-193.

[4] HARVEY J E, CHOI N, KRYWONOS A, *et al*.. Image degradation due to scattering effects in two-mirror telescopes[J]. *Opt. Eng.*, 2010, 49(6): 063202.

[5] KOZHEVNIKOV I V, ASADCHIKOV V E, ALAUDINOV, *et al*.. X-ray investigations of super smooth surfaces[J]. *Proceedings of SPIE*, 1995, 2453: 141-153.

[6] DE KORTE P A J, LAINE R. Assessment of surface roughness by X-ray scattering and differential interference contrast microscopy[J]. *Applied Optics*, 1979, 18(2): 236-242.

[7] ZANAVESKIN M L, GRISHCHENKO Y V, TOLSTIKHINA A L, *et al*.. The surface roughness investigation by the atomic force microscopy, X-ray scattering, and light scattering[J]. *Proceedings of SPIE*, 2006, 6260: 62601A-1-62601A-10.

[8] RUPPE C, DUPARRE A. Roughness analysis of optical films and substrates by atomic force microscopy[J]. *Thin Solid Films*, 1996, 288(1-2): 8-13.

[9] VINOGRADOV A V, ZOREV N N, KOZHEVNIKOV I V, *et al*.. X-ray scattering by highly polished surfaces[J]. *Journal of Experimental and Theoretical Physics*, 1988, 67(8): 1631-1638.

[10] ASADCHIKOV V E, KOZHEVNIKOV I V, KRIVONOSOV Y S, *et al*.. Application of X-ray scattering technique to the study of super smooth surfaces[J]. *Nucl. Instr& Meth A*, 2004, 530(3): 575-595.

[11] 王永刚, 孟艳丽, 马文生, 等. 掠入射 X 射线散射法测量超光滑表面[J]. 光学 精密工程, 2010, 18(1): 60-68.
WANG Y G, MENG Y L, MA W SH, *et al*.. Measurement of super-smooth surface by grazing X-ray scattering method [J]. *Opt. Precision Eng.*, 2010, 18(1): 60-68. (in Chinese)

[12] ANDREY KROYWONOS. Predicting surface scatter using a linear systems formulation of non-paraxial scalar diffraction [D]. Central Florida: University of Central Florida, 2006: 178-180.

[13] KRYWONOS A, HARVEY J E, CHOI N. Linear systems formulation of scattering theory for roughsurfaces with arbitrary incident and scattering angles[J]. *J. Opt. Soc. Am. A*, 2011, 28(6): 1121-1138.

[14] DITTMAN M G. K-correlation power spectral density and surface scatter model[J]. *Proceedings of SPIE*, 2006, 6291: 6290R.

[15] ZEMAX Development Corp. *ZEMAX Manual: Optical Design Program User's Guide*[M]. Sandiego: ZEMAX Development Corp, 2009: 331-446.

作者简介:

ZHANG Ya-chao (1989—), is a Ph. D. student at Changchun Institute of Optics, Fine Mechanics and Physics, Chinese Academy of Sciences. His current research interests include the calibration of X-ray optical system. E-mail: zyc198902@126.com

CHEN Bo (1961—), is a professor in the Chinese Academy of Sciences. He received his Ph. D. degree from Changchun Institute of Optics, Fine Mechanics and Physics, Chinese Academy of Sciences in 2003. His current research interests include soft X-ray and extreme ultraviolet sources, radiation metrology and optical space instruments. E-mail: chenb@ciomp.ac.cn